J. Fluid Mech. (2003), *vol.* 493, *pp.* 363–378. © 2003 Cambridge University Press
DOI: 10.1017/S0022112003006001 Printed in the United Kingdom

Particle migration in pressure-driven flow of a Brownian suspension

By MARTIN FRANK[1], DOUGLAS ANDERSON[1], ERIC R. WEEKS[1] AND JEFFREY F. MORRIS[2]†

[1]Department of Physics, Emory University, Atlanta, GA 30322-2430, USA

[2]School of Chemical Engineering, Georgia Institute of Technology, Atlanta, GA 30332-0100, USA

(Received 10 September 2002 and in revised form 13 June 2003)

Shear-induced migration of 2 μm diameter spherical colloidal particles flowing through rectangular channels (50 μm × 500 μm cross-section) is studied by confocal microscopy. The confocal microscope allows imaging of the flowing particles far from the walls of the channel, at particle velocities up to 8000 μm s^{-1}. The particle volume fraction is varied from $\phi = 0.05$ to 0.34, and the flow rate is also varied, which results in a bulk Péclet number (Pe_B) which varies by two orders of magnitude. Concentration profiles are measured across the narrow dimension of the channel; particles at the larger volume fractions migrate toward the centreline, with the migration progressively stronger as Pe_B increases. The flow has been analysed using an existing mixture flow model under the assumption of fully developed flow and a proposed constitutive law which describes the suspension normal stresses as a function of both ϕ and the local Péclet number, Pe, the latter being defined as a variable quantity through the local shear rate. Shear thinning and shear thickening are not included. Comparisons made with the experimental data indicate that the dependence of the extent of migration upon Pe_B is captured well but discrepancies arise, at least in part because the assumption of full development is not valid for these experiments.

1. Introduction

Bulk migration of particles has been well-documented for non-Brownian suspension flows. However, there has been no experimental study of which we are aware describing this migration phenomenon in suspensions made up of particles sufficiently small to undergo observable Brownian motion. This work considers migration of particles in channel flow of a Brownian suspension. Experimental observations obtained by confocal microscopy of the particle volume fraction, ϕ, of a suspension of micron-radius particles are compared with predictions of a bulk flow model. The flow model accounts for particle migration through the influence of the particle-induced normal stresses following the approach of Nott & Brady (1994) in the form outlined by Morris & Boulay (1999).

The migration of non-Brownian particles in channel flow of a suspension has been well-studied, both by experiment (Koh, Hookham & Leal 1994; Lyon & Leal 1998) and combined simulation and modelling (Nott & Brady 1994; Morris & Brady 1998). The channel flow studies are part of a substantial body of work on the bulk flow

† To whom correspondence should be addressed. Present address: Halliburton Energy Services, 2600 S. 2nd Street; Duncan, OK 73536, USA; jeff.morris2@halliburton.com.

and migration in non-Brownian suspensions, an area of active study for well over a decade, beginning with the work of Leighton & Acrivos (1987). There has been little attention given to migration in Brownian suspensions. A notable exception is the modelling study of Buyevich & Kapsbov (1999), which also considered channel flow. Buyevich & Kapsbov analysed the problem in the same framework that we shall use, with migration driven by normal stresses; however, the constitutive model for the normal stresses was considerably different from that proposed here, as discussed in § 3.

The rheology of Brownian suspensions has been studied by numerous authors and aspects of the rheology are well-understood (Russel, Saville & Schowalter 1989; Brady 1993). Hard-sphere dispersions may be characterized, if monodisperse, by a Péclet number, Pe, and the particle volume fraction, ϕ. The Péclet number is the ratio of shear-driven to thermal (Brownian) motion at the particle scale. The behaviour of the steady shear viscosity as a function of Pe and ϕ has been studied experimentally (van der Werff & de Kruif 1989) and by simulation (Phung, Brady & Bossis 1996) with good quantitative agreement between the two throughout the shear-thinning regime. For normal stresses in Brownian suspensions, experimental data are, unfortunately, lacking. Theory and simulation thus provide the best information. Brady & Vicic (1995) and Brady & Morris (1997) have analysed, respectively, the small- and large-Pe limits of the suspension microstructure and obtained predictions of the normal stresses of dilute suspensions under these conditions, with extension of the results to large ϕ by scaling arguments. The results of these asymptotic theories have been used here to develop the form of a single constitutive law for the suspension normal stresses for all Pe and ϕ. The form has been found to be satisfactory in reproducing the observed behaviour as a function of Pe in the simulations of concentrated suspensions by Phung *et al.* (1996) and by Foss & Brady (2000). It is interesting to note that the variation of the normal stresses with Pe in these concentrated systems is found even in dilute suspensions as shown by the theoretical work based on the pair-particle Smoluchowski equation by Bergenholtz, Brady & Vicic (2002).

We experimentally study the flow of Brownian particles using confocal microscopy to directly image the particle concentrations and motions. The migration can be clearly seen in figure 1, which shows a sequence of images from a suspension with bulk solid volume fraction $\phi_{\text{bulk}} = 0.22$ with flow rate increasing from left to right. There have been prior experimental examinations of migration in non-colloidal suspension flow, and several of these have made use of laser-Doppler velocimetry (Koh *et al.* 1994; Lyon & Leal 1998). The details of our experiments based on the rather different technique of confocal microscopy are presented in § 2. The model is presented in § 3. The modelling predictions under an assumption of fully developed flow, along with a comparison with the experiments, conclude the work. The comparison indicates that the model is successful in capturing both the ϕ and Pe dependence of the migration phenomenon, although the assumption of full development appears to be invalid for these experiments.

2. Experiment

We study the flow of colloidal particles composed of poly-(methylmethacrylate), sterically stabilized by a thin layer of poly-12-hydroxystearic acid (Antl *et al.* 1986). The particles are slightly charged hard spheres with an effective radius $a = 1.1\,\mu\text{m}$, and are labelled with fluorescent rhodamine dye and suspended in a cyclohexylbromide/decalin mixture which matches the index of refraction and the

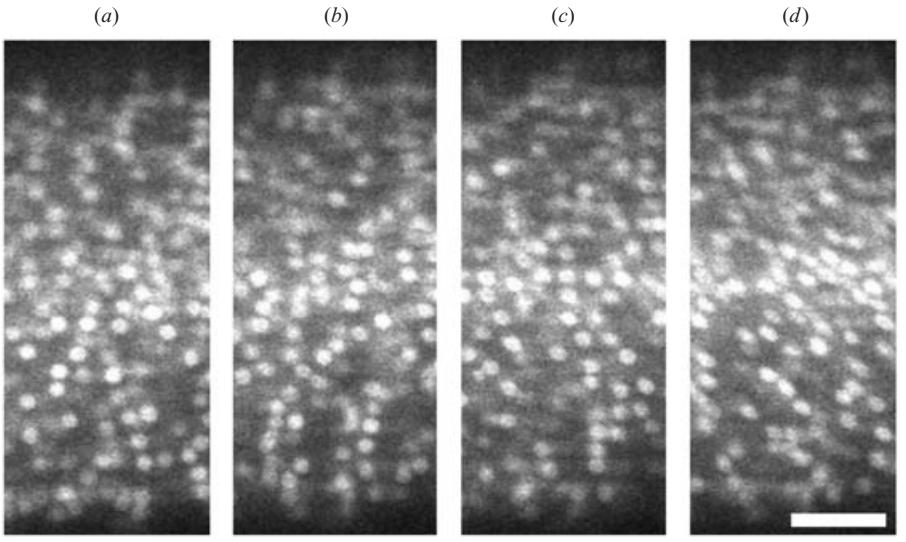

FIGURE 1. Pictures taken with the confocal microscope of flowing suspension at $\phi_{\text{bulk}} = 0.22$ at increasing flow rates (Q) ((*a*): $Q = 0.125\,\mu\text{l}\,\text{min}^{-1}$, (*b*) $Q = 0.25\,\mu\text{l}\,\text{min}^{-1}$, (*c*) $Q = 0.50\,\mu\text{l}\,\text{min}^{-1}$, (*d*) $Q = 1.0\,\mu\text{l}\,\text{min}^{-1}$; Péclet numbers: 69, 140, 280, and 550). It is evident that the migration effect becomes more pronounced with higher flow rate. The scale bar has a size of 10 μm. The particles are flowing from right to left.

density. The particle volume fraction is defined based on the number density n and the effective radius as $\phi = 4\pi a^3 n/3$.

The flow chamber is a long rectangular glass channel (Friedrich & Dimock) of $50 \times 500\,\mu\text{m}^2$ cross-section, connected on each side to a Teflon tube (Small Parts Inc.). The glass channel is mounted onto a slide for mechanical stability. We use a 100 μl gas-tight syringe (Hamilton) placed on a syringe pump (kd Scientific) to drive our flows. Initially the syringe, Teflon tube and glass channel are flushed with acetone and dried before the data acquisition. Before acquisition, we flow the suspension at a rate of $2.0\,\mu\text{l}\,\text{min}^{-1}$ for at least 2 minutes, to fill the sample chamber and provide simple initial conditions. Next, the flow rate (Q) is decreased to $Q = 0.125\,\mu\text{l}\,\text{min}^{-1}$, and subsequently doubled for each successive reading up to a maximum flow of $Q = 8.0\,\mu\text{l}\,\text{min}^{-1}$. At each flow rate, we wait an appropriate amount of time so that all of the particles within the glass flow channel have entered the channel at the given flow rate. The entry of the glass flow channel is 2.6 cm from the microscope field of view, providing a ratio of flow length to the narrow dimension of the channel of 520. Longer channels with similar dimensions were not available, limiting our ability to examine flows which required longer distances to fully develop, as discussed below.

We utilize a fast confocal microscope (ThermoNoran), so that we can scan hundreds of flowing particles at a high acquisition rate, and resolve them despite their fast motion. The confocal microscope uses a laser to excite fluorescence in the colloidal particles, and uses a spatial filtering technique to produce clean optical sections from deep within the sample (Dinsmore *et al.* 2001). This technique allows a sharper field of view and a better optical resolution. The confocal microscope is attached to a Leica inverted microscope, using a $100\times/1.4$ N.A. objective, with a field of view of $63 \times 67\,\mu\text{m}^2$. Our confocal microscope is capable of acquiring images at 120 frames each second, and thus we can see particles flowing at speeds of up to

$8000\,\mu m\,s^{-1}$, despite the fact that the particles are only within the field of view for fractions of a second. In figure 1 we present images of particles flowing at speeds of $O(100\text{–}1000)\,\mu m\,s^{-1}$. The image quality is adequate to determine both velocity and concentration profiles, despite the fact that at velocities above $1000\,\mu m\,s^{-1}$ the particle images are distorted significantly.

We quantify the flow rate with the dimensionless Péclet number, which conceptually is the ratio of the time required for Brownian diffusion to move a particle its own size, $a^2/D_0 = a^2/(kT/6\pi\eta_0 a)$, to the time required for shear flow to move it the same distance, $\dot{\gamma}^{-1}$, yielding

$$Pe = \frac{6\pi\eta_0\dot{\gamma}a^3}{kT}. \tag{1}$$

To characterize an experiment, the shear rate is defined $\dot{\gamma} = u_{max}/(H/2)$, using $H = 50\,\mu m$ as the narrow dimension of the flow chamber; the resulting parameter is denoted Pe_B to indicate that it describes the bulk, rather than local, conditions, a distinction which will be important later. In the above expressions, η_0 is the viscosity of the solvent, u_{max} is the maximum axial velocity of the suspension, k Boltzmann's constant and T temperature.

To determine the velocity profile, we image the flow by focusing through the sidewall of the glass channel; see view (*b*) of figure 2. The microscope is slowly scanned through the entire depth of the channel (from $y = 0\,\mu m$ to $y = 50\,\mu m$) while acquiring a sequence of images. By cross-correlating each successive pair of images, we are able to determine the flow velocity as a function of y. The flow profile is nearly parabolic, as seen in the inset of figure 3 for $Q = 1.4\,\mu l\,min^{-1}$ ($Pe_B = 770$), implying that the shear rate varies almost linearly with y and that the maximum velocity used in defining Pe may be related to the mean velocity, $\bar{u}$, as $u_{max} \doteq 3\bar{u}/2$. For our higher concentrations at elevated flow rates, particle migration results in a slight deviation from a parabolic toward a more plug-like profile, and this is illustrated in the main plot of figure 3 which shows the deviation from a parabolic (Poiseuille) profile for both the experimentally measured velocity and the model predictions at $Pe_B = 770$. The experimental and model $\phi(y)$ profiles associated with these velocity profiles may be estimated by interpolation between the $Pe_B = 550$ and $Pe_B = 4400$ results at $\phi_{bulk} = 0.22$ in figure 4 and figure 6, respectively. The model predicts a more rapid shearing near the wall owing to depletion of particles and reduced effective viscosity, and thus $v - v_p > 0$ adjacent to the wall, with a crossover to a blunted profile with $v - v_p < 0$ near the centreline. The experimental data are observed to have a negative deviation from a parabolic profile near the centreline, but the deviation is considerably smaller than the model predicts.

To determine the concentration profile, we image the flow by utilizing a flow chamber rotated 90° and focusing through the short wall of the glass channel; see view (*a*) of figure 2. We acquire 1000 images at a distance $50\,\mu m$ from the wall (10% into the flow chamber). We create a composite image by averaging these 1000 images; the composite image is brighter where more particles were seen. The composite image is essentially uniform in intensity along the direction of flow, so this image is averaged over this direction (the x-direction) to yield an image intensity profile as a function of y. To correct for optical effects, the intensity profile is then normalized by dividing by a similar profile obtained in the case of no flow ($Q = 0$), then rescaled to ensure that the average ϕ equals ϕ_{bulk}, thus producing the concentration profile as a function of y.

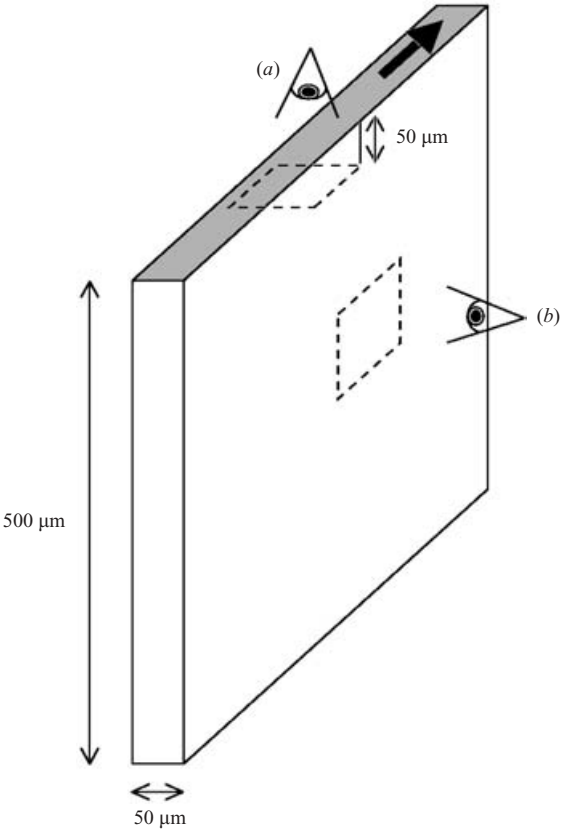

FIGURE 2. Sketch of the experimental flow chamber; the bold arrow indicates the flow direction. Concentration profiles were obtained by looking through the top (*a*) at a fixed distance (50 μm) from the top wall. Velocity profiles were taken by scanning a horizontal plane through the side (*b*) of the chamber, across the 50 μm width of the channel.

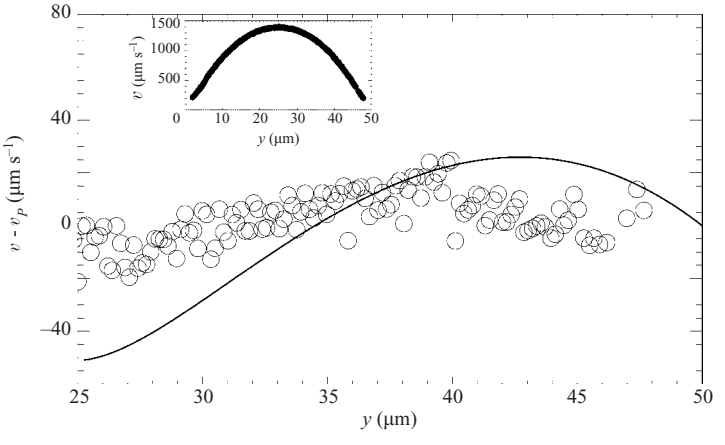

FIGURE 3. The velocity profile as a function of the distance across the channel at an average volume fraction $\phi_{\text{bulk}} = 0.22$ and a flow rate of $Q = 1.4\,\mu\text{l}\,\text{min}^{-1}$ ($Pe_{\text{B}} = 770$). The inset shows the experimentally measured velocity. The main plot shows, for half of the channel, the deviation from a parabolic (Poiseuille) profile for both experiment (symbols) and the model (line) at these same conditions. Measurement error is less than $20\,\mu\text{m}\,\text{s}^{-1}$.

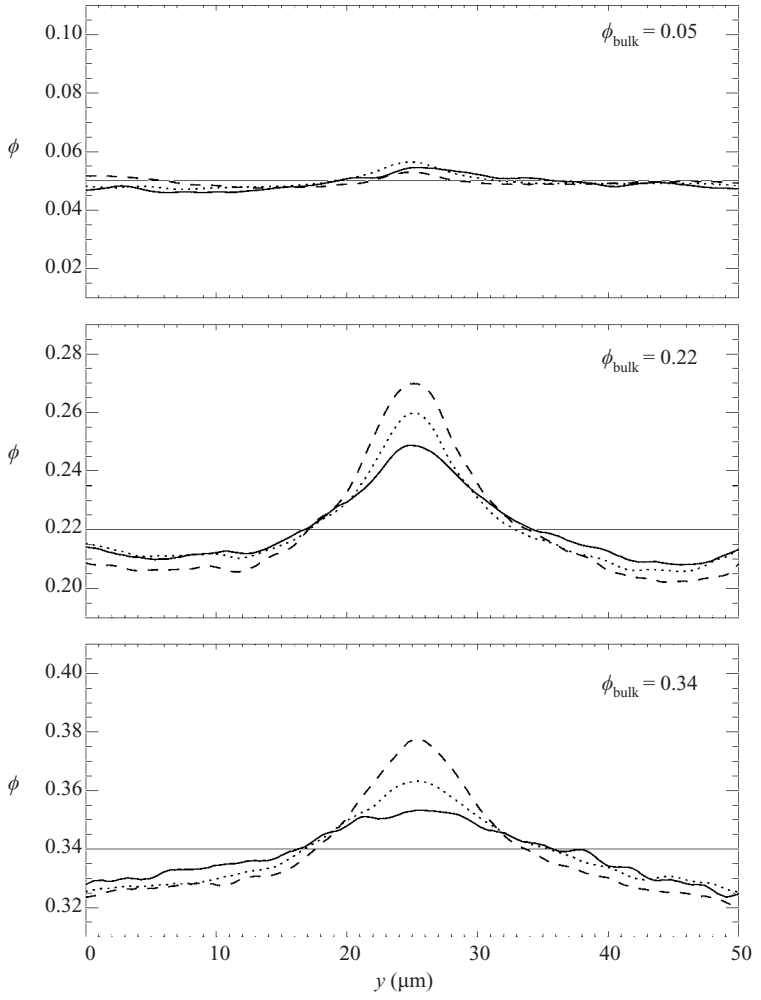

FIGURE 4. Plots of the local volume fraction ϕ as a function of the distance across the channel for an average volume fraction of $\phi_{bulk} = 0.05$, 0.22, and 0.34 at flow rates of $0.125\,\mu l\,min^{-1}$ (solid line; $Pe_B = 69$), $1.0\,\mu l\,min^{-1}$ (dotted; $Pe_B = 550$), and $8.0\,\mu l\,min^{-1}$ (dashed; $Pe_B = 4400$). The upturns at the edges ($y \approx 0\,\mu m$ and $y \approx 50\,\mu m$) are due to optical effects at the channel walls. For $5 < y < 45\,\mu m$, the errors in $\phi(y)$ are less than 0.01, and are due to imaging limitations.

In figure 4 we can see that at low volume fraction, $\phi_{bulk} = 0.05$, there is only a slight increase in concentration in the centre. Although the variation observed is sufficient to indicate that shear-induced particle migration has occurred, the profile does not appear to change over a wide range of Pe_B and hence little confidence can be placed in the detailed form of the concentration profile. As discussed in § 4, the flow is probably not completely developed even for the most concentrated suspension studied, and certainly is not expected to be for this volume fraction. Weak migration for $\phi_{bulk} = 0.05$ is not surprising as will be seen from the modelling of § 3.2: migration is due to shear-induced particle interactions scaling as ϕ^2, and at low volume fractions where particles are widely distributed such interactions are a weak effect. Although the variations with Pe_B of the peak height of $\phi(y)$ for $\phi_{bulk} = 0.05$ are within the

uncertainty of the measurement, the qualitative increase in $\phi(y)$ near the channel centre is, nonetheless, reproducible in our experiments at low volume fractions.

When the volume fraction increases to $\phi_{\text{bulk}} = 0.22$ and $\phi_{\text{bulk}} = 0.34$, the increase in local concentration is significantly larger in the middle of the channel, as seen in figure 4. This becomes increasingly evident at higher flow rates (higher Pe_{B}). The enhanced particle migration with increasing flow rate is also clearly shown in the raw data of figure 1. We have checked that 50 μm is sufficiently far from the top wall of the capillary channel; the concentration profile does not change significantly for measurements taken more than 30 μm below the top wall (see figure 2*a*).

3. Flow analysis and model

In § 3.1, we develop the equation needed to describe the particle migration relative to the bulk flow, given in general form by (6) below and in the form for fully developed channel flow used for comparison with the experiments by (8). These equations require a rheological model which accounts for the normal stresses resulting from the particles, and the rheological constitutive model expressed by (11)–(13) appears at the beginning of § 3.2. This is followed by the rationale for the specific form of the constitutive law.

3.1. *Governing equations*

Following prior work (Nott & Brady 1994; Morris & Boulay 1999), the conservation equations for particle mass (volume) and momentum of a neutrally buoyant low-Reynolds-number suspension are given, respectively, by

$$\frac{\partial \phi}{\partial t} + \nabla \cdot (\boldsymbol{U}\phi) = 0, \tag{2}$$

and

$$0 = \nabla \cdot \boldsymbol{\Sigma}^P + n\langle \boldsymbol{F}^H \rangle, \tag{3}$$

where $\boldsymbol{U}$ is the local ensemble-average velocity of the particle phase, $\langle \boldsymbol{F}^H \rangle$ is the average drag force on an individual particle, and we recall that n is the particle number density. The particle contribution to the bulk stress is denoted $\boldsymbol{\Sigma}^P$, and may include hydrodynamic, interparticle force, and Brownian components (Brady 1993). The particle stress model is presented in § 3.2.

Under low-Reynolds-number conditions, the hydrodynamic force $\boldsymbol{F}^H$ appearing in (3) is linearly related to the relative velocity between the particles and bulk suspension. A simple means of expressing this is

$$n\boldsymbol{F}^H = -6n\pi\eta_0 a f^{-1}(\phi)(\boldsymbol{U} - \langle \boldsymbol{u} \rangle) = -\frac{9\eta_0}{2a^2}\phi f^{-1}(\phi)(\boldsymbol{U} - \langle \boldsymbol{u} \rangle), \tag{4}$$

where $\langle \boldsymbol{u} \rangle$ is the ensemble-average velocity of the bulk suspension, and $f(\phi) \leqslant 1$ is the sedimentation hindrance function, the ratio of the sedimentation velocity of a uniform sedimentation at ϕ to the Stokes settling velocity of an isolated sphere. In the absence of a migration flux, the drag force vanishes, and our consideration of the fully developed ϕ profile will satisfy this condition.

The coupling between the particle migration flux and the suspension stress becomes clear when we insert (4) to (3) and solve for the particle flux,

$$\phi \boldsymbol{U} = \phi \langle \boldsymbol{u} \rangle + \frac{2a^2}{9\eta} f(\phi) \nabla \cdot \boldsymbol{\Sigma}^P, \tag{5}$$

which when substituted to (2) yields

$$\frac{\partial \phi}{\partial t} + \langle \boldsymbol{u} \rangle \cdot \nabla \phi = -\frac{2a^2}{9\eta} \nabla \cdot [f(\phi) \nabla \cdot \boldsymbol{\Sigma}^P]. \tag{6}$$

This indicates that the particle-induced rheology drives migration in a suspension flow.

The channel flow studied experimentally in this work is steady. Labelling the axial coordinate x and the cross-stream coordinate for the narrow dimension of the channel y, ϕ is governed by

$$\langle \boldsymbol{u} \rangle \cdot \nabla \phi = -\frac{2a^2}{9\eta} \frac{\partial}{\partial y} \left(f(\phi) \frac{\partial \Sigma^P_{yy}}{\partial y} \right). \tag{7}$$

Here, we will consider only the fully developed state, where the cross-stream flux vanishes and $\langle \boldsymbol{u} \rangle \cdot \nabla \phi = u_x \partial \phi / \partial x = 0$. Consequently, the fully developed $\phi(y)$ may be determined from

$$\frac{\partial \Sigma^P_{yy}}{\partial y} = 0 \quad \text{(fully-developed)} \tag{8}$$

augmented by the axial momentum equation,

$$0 = -\frac{\mathrm{d}P(x)}{\mathrm{d}x} + \frac{\partial}{\partial y} \left(\eta_0 \eta_s(\phi) \frac{\partial u_x}{\partial y} \right) \tag{9}$$

from which we determine $\dot{\gamma} \equiv |\partial u_x / \partial y|$. The solution procedure is presented in § 3.3.

3.2. *Bulk stress model at finite Pe*

To predict the suspension flow inclusive of particle migration, (8) indicates the need for a rheological model which captures the salient features of the normal stress components. The present experiments involve micron-scale particles and the shear rate varies across the channel, and thus the role of Brownian motion at variable *Pe* must be included. For the shear stress, we use a generalized Newtonian model given by $\Sigma_{12} = \eta_0 \eta_s(\phi) \dot{\gamma}$, with $\eta_s = 1 + 2.5\phi(1 - \phi/\phi_{\max})^{-1} + 0.1\phi^2(1 - \phi/\phi_{\max})^{-2}$ (Morris & Boulay 1999); the results presented would not be qualitatively altered by taking η_s as the well-known form from Krieger (1972). To maintain simplicity and a focus on the influence of normal stresses, we include neither shear thinning nor shear thickening. The neglect of these features should, however, have little effect upon the predictions made for comparison with the experiments, because both phenomena are found to be mild for the particle fractions considered here. From the simulations of Phung *et al.* (1996), the results of which are in quantitative agreement with the experimental results of van der Werff & de Kruif (1989) in the shear-thinning regime, the effective viscosity has only about 30% variation between the extreme values for $\phi = 0.37$ over a range of $0 < Pe \leqslant 10^4$. Our experiments have measured local concentrations of $\phi < 0.4$.

We turn now to the normal stress model, defined for simple-shear flows. The normal stresses are labelled using the standard convention with flow, gradient, and vorticity being the 1, 2, and 3 directions, respectively. Although only the normal stress $\Sigma^P_{22} = \Sigma^P_{yy}$ is needed for the channel flow, for completeness we present a model for all normal stress components. The normal stresses are taken to be a sum of thermally driven and shear-driven components, respectively the first and second terms on the right of

$$\Sigma^P_{ii} = \Sigma^T_{ii} + \Sigma^{\dot{\gamma}}_{ii}, \tag{10}$$

where the subscript ii indicates a normal stress component and not an implied summation. Assuming the thermal contribution, scaling as nkT, is both isotropic and independent of Pe, the normal stress model we propose may be written

$$\frac{\Sigma_{ii}^{P}}{-kT/\frac{4}{3}\pi a^3} = a(\phi) + \frac{2\,Pe}{9}\left[b_i^{-1}(\phi, Pe) + c_i^{-1}(\phi)\right]^{-1}, \tag{11}$$

with the scaling by a characteristic thermal stress of $-kT/(4\pi a^3/3)$. This scaling, rather than $\eta_0\dot{\gamma}$, is taken because it provides a reduction to dimensionless form based upon quantities which will remain constant in the channel flow of interest. In (11), the first term on the right-hand side represents the isotropic thermal stress, while the final term (involving the subscripted b_i and c_i) models the shear-driven anisotropic normal stresses. The thermal stress contribution is modelled as

$$a(\phi) = 3\phi\left(1 - \frac{\phi}{\phi_{\max}}\right)^{-1}, \tag{12}$$

based on the work of Woodcock (1981) (see also Russel *et al.* 1989, section 10.5) while the shear-driven stress functions are

$$b_i(\phi, Pe) = A\lambda_i{}^{B} Pe\phi\left(1 - \frac{\phi}{\phi_{\max}}\right)^{-3}, \quad c_i(\phi) = \lambda_i^{H}\eta_n(\phi), \tag{13}$$

with $\eta_n(\phi) = 0.75(\phi/\phi_{\max})^2(1 - \phi/\phi_{\max})^{-2}$ the 'normal stress viscosity' suggested by Morris & Boulay (1999) for non-Brownian suspensions.

The form of the shear-driven stress is such that it asymptotes to appropriate forms at small Pe ($b_i^{-1} \gg c_i^{-1}$) and large Pe ($b_i^{-1} \ll c_i^{-1}$), with the Péclet number at which a transition from low- to large-Pe behaviour occurs determined by A. The parameter A and the anisotropy factors λ_i^B and λ_i^H are the primary variable parameters for fitting the constitutive model (11) to available data. It is these anisotropy factors which allow modelling of normal stress differences predicted analytically and observed from simulation in the limit of a Brownian or small-Pe (λ_i^B) or a hydrodynamically dominated (λ_i^H) suspension. The anisotropy factors depend also upon volume fraction, as noted below.

To use the stress law (11)–(13) in a flow with variable shear rate, the Péclet number must represent the local ratio of shearing to thermal forces. In the case of the channel flow, $Pe = Pe_{\mathrm{B}} \times (2|\bar{y}|)$ where we recall that

$$Pe_{\mathrm{B}} = \frac{6\pi\eta_0\bar{\dot{\gamma}}a^3}{kT}, \quad \bar{\dot{\gamma}} = \frac{u_{\max}}{H/2}.$$

The dimensionless cross-stream coordinate measured from the centreline of the channel is $\bar{y} = y/(H/2)$. The local Pe is proportional to the local shear stress, which is linear in $\bar{y}$, and has mean value Pe_{B}.

Prior modelling of suspension normal stresses for purposes similar to ours has been proposed by Buyevich & Kapsbov (1999). In their flow analysis, Buyevich & Kapsbov found that the particle distribution is governed by the balance (8), consistent with work using the 'suspension-balance model' (Nott & Brady 1994; Morris & Brady 1998). There thus is consensus among several studies addressing the channel flow of suspensions that the cross-stream normal stresses drive the migration. However, Buyevich & Kapsbov modelled the Brownian normal stresses as strictly isotropic while modelling the hydrodynamic normal stresses $\Sigma_{ii}^{P,H} \sim \dot{\gamma}^2$ for all Pe. The modelling of isotropic Brownian normal stresses has little impact upon the channel flow, but is

inconsistent with the theory of Brady & Vicic (1995) and Bergenholtz *et al.* (2002). Quadratic dependence of the hydrodynamic normal stresses upon $\dot{\gamma}$ is valid for asymptotically small Pe, whereas the stresses at large Pe are viscous and thus linear in $\dot{\gamma}$. This is theoretically described for the normal stresses in the theory of Jeffrey, Morris & Brady (1993) and Brady & Morris (1997), borne out reasonably well by experiments (where surface interactions and wall slip may introduce a different rate dependence) of Gadala-Maria (1979) and Leighton & Rampall (1993), and confirmed by simulations of Phung *et al.* (1996).

3.2.1. *Basis and form of constitutive model for* $\boldsymbol{\Sigma}^P$

As the prior discussion indicates, the modelling of normal stresses used in this study was developed to be consistent with the best available understanding of this aspect of colloidal rheology, while leaving aside the issue of shear thinning and thickening. Here we address the basis for the normal stress modelling given by (11)–(13). The proposed constitutive model is based primarily upon microstructural analyses and simulation results, both of which provide information on the Pe-dependence. Experimental normal stress difference information is sparse, but the available results for non-colloidal suspensions (e.g. Zarraga, Hill & Leighton 2000) are largely consistent with the modelling used here for $Pe \gg 1$.

In the limit $Pe \to 0$, Brady & Vicic (1995) extended the small-Pe microstructural analysis of Batchelor (1977) to $O(Pe^2)$ to determine the normal stresses analytically for $\phi \to 0$. These authors also applied a scaling analysis based on the work of Brady (1993) to develop predictions for concentrated suspensions ($\phi \to \phi_{\max}$) at small $\bar{Pe} = PeD_0/D_0^s(\phi) \to 0$; here $D_0 = kT/6\pi\eta_0 a$ is the self-diffusion while $D_0^s(\phi)$ is the short-time self-diffusion coefficient given by kT times the average particle mobility. The reduction of mobility of particles as $\phi \to \phi_{\max}$, with $D_0^s(\phi) \sim 0.85(1 - \phi/\phi_{\max})$, increases the relative strength of hydrodynamics at a given Pe and this is reflected in $\bar{Pe}$. The dilute predictions are

$$\frac{N_1}{\eta_0\dot{\gamma}} = 0.899\phi^2 Pe, \frac{N_2}{\eta_0\dot{\gamma}} = -0.788\phi^2 Pe, \quad \frac{\Pi}{nkT} = 1 + 4\phi + 0.156\phi Pe^2, \tag{14}$$

plus terms of $O(\phi Pe^2)$; $\Pi = -\frac{1}{3}\boldsymbol{I} : \boldsymbol{\Sigma}^P$. For concentrated suspensions, the predictions are

$$\left.\begin{aligned} &\frac{N_1}{\eta_0\dot{\gamma}} = 0.6\left(1 - \frac{\phi}{\phi_{\max}}\right)^{-3} Pe, \quad \frac{N_2}{\eta_0\dot{\gamma}} = -0.42\left(1 - \frac{\phi}{\phi_{\max}}\right)^{-3} Pe, \\ &\frac{\Pi}{nkT} = 2.9\left(1 - \frac{\phi}{\phi_{\max}}\right)^{-1} + 0.37\left(1 - \frac{\phi}{\phi_{\max}}\right)^{-3} Pe^2, \end{aligned}\right\} \tag{15}$$

plus terms of $O(\bar{Pe}^2)$. The results are stated in terms of Pe for simplicity of further expressions. Noting that $nkTPe = \frac{9}{2}\phi\eta_0\dot{\gamma}$ in the expressions for Π, the influence of weak shearing is predicted to scale as $\Sigma_{ii}^{\dot{\gamma}} \sim \eta_0\dot{\gamma}\phi^2 Pe$ for $\phi \to 0$ and as $\Sigma_{ii}^{\dot{\gamma}} \sim \eta_0\dot{\gamma}(1 - \phi/\phi_{\max})^{-3} Pe$ for $\phi \to \phi_{\max}$. The function $a(\phi)$ is deduced from the leading term on the right-hand side of the expression for Π, while $b_i(\phi, Pe)$ is deduced from the shear-driven components of (14) and (15).

In the limit of large Pe, Brady & Morris (1997) analysed a strongly sheared dilute suspension of near-hard spheres in planar extensional flow, showing that asymmetry of the pair microstructure resulting from Brownian motion or short-ranged interparticle forces results in finite normal stresses in the limit $Pe \to \infty$, with $N_2 \sim \eta_0\dot{\gamma}\phi^2$. In the extensional flow of a simple shear $u_1 = \dot{\gamma}x_2$, $N_1 = \Sigma_{11} - \Sigma_{22} = 0$ by symmetry, but

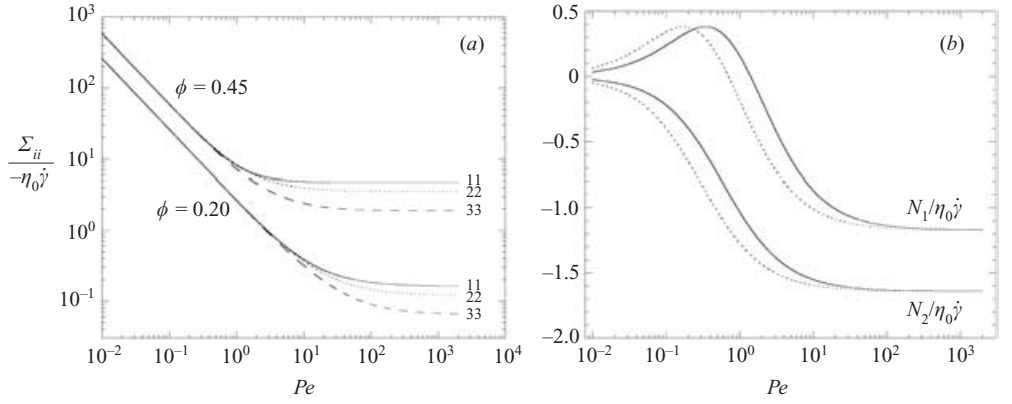

FIGURE 5. Normal stress dependence on Pe_B based on the proposed constitutive model: (*a*) the individual normal stresses for $A = 0.2$ at $\phi = 0.2$ and $\phi = 0.45$; (*b*) the first and second normal stress differences at $\phi = 0.45$ for $A = 0.2$ (solid lines) and $A = 0.4$ (dashed lines).

this symmetry is broken in simple-shear flow to yield a finite N_1, as shown for dilute suspensions by Bergenholtz *et al.* (2002). A constitutive model for prediction of concentrated non-colloidal suspension flows inclusive of anisotropic normal stresses, with $\Sigma_{ii}^P \sim \eta_0\dot{\gamma}\phi^2(1-\phi/\phi_{max})^{-2}$ as $\phi \to \phi_{max}$, has been developed by Morris & Boulay (1999) and found successful for curvilinear flows where normal stress differences play a critical role. The function c_i is chosen so that the proposed normal stress model agrees with that of Morris & Boulay in the limit $Pe \to \infty$ and $\phi \to \phi_{max}$. For smaller ϕ, simulation data indicate that the stress anisotropy must be modified.

Theory (Brady & Vicic 1995) and simulation (Phung *et al.* 1996; Morris & Katyal 2002) indicate that the anisotropy factors vary with both ϕ and Pe. For channel flow, only Σ_{22}^P is relevant and results presented here are unaffected by the anisotropy factors. The modelled normal stress differences have the general structure of those found in simulation by Phung *et al.* (1996) for $\phi = 0.45$ using $A = 0.2$–0.3, with the anisotropy factors $[\lambda_1^H = 1,\ \lambda_2^H = 0.75,\ \lambda_3^H = 0.4]$ and $[\lambda_1^B = 1, \lambda_2^B = 1.8, \lambda_3^B = 1.2]$. For small ϕ and $Pe \ll 1$, $[\lambda_1^B = 1, \lambda_2^B = 3.5, \lambda_3^B = 1.3]$ are found from results of Brady & Vicic (1995).

In figure 5(*a*), we plot the normal stress model in the form of $\Sigma_{ii}^P/(-\eta_0\dot{\gamma})$ as a function of Pe at $\phi = 0.2$ and 0.45, both for $A = 0.2$. Because the rate-dependent and anisotropic normal stresses have a stronger divergence than the isotropic Brownian contribution for $\phi \to \phi_{max}$, the stress exhibits anisotropy at smaller Pe with increasing ϕ. In figure 5(*b*), the normal stress differences scaled by $\eta_0\dot{\gamma}$ are plotted as a function of Pe for $\phi = 0.45$ for $A = 0.2$ and $A = 0.4$. The model captures not only the basic form but also the transition from low- to high-Pe behaviour; the shift of the transition to smaller Pe at larger A is readily rationalized by considering the form of b_i. We use $A = 0.4$ in the predictions for comparison with experiment, although the simulation data at $\phi = 0.45$ from Phung *et al.* (1996), with corrections noted by Foss & Brady (2000), may be better represented by $A = 0.2$. Key features are that N_1 goes through a maximum at Pe near unity and then becomes negative, while N_2 begins negative and becomes increasingly so as Pe grows. These features have been shown by Bergenholtz *et al.* (2002) to occur in dilute systems, confirming that essential aspects of the microstructure giving rise to the normal stresses may be understood at the pair level, although simulation data show that the stress anisotropy as $Pe \to \infty$

varies substantially with ϕ (Morris & Katyal 2002) and thus the ratio of $|N_1/N_2|$ for $\phi = 0.45$ would not be appropriate at small ϕ. The influence of A upon the predicted migration in fully developed channel flow is considered in § 4.

3.3. *Model solution for developed channel flow*

While the solution of (6) for the general case may prove difficult, the fully developed state is governed by

$$\frac{\partial \Sigma_{yy}^{P}}{\partial y} = 0 \quad \text{or} \quad \Sigma_{yy}^{P} = \Pi(0), \tag{16}$$

indicating that the normal stress across the channel is equal to the osmotic pressure at the channel centreline. Inserting to (16) the dimensionless form of $\Sigma_{yy}^{P} = \Sigma_{22}^{P}$ given by (11), we obtain a relationship between $\partial\phi/\partial\bar{y}$ and $\partial Pe/\partial\bar{y}$ involving only information locally available at the position. This information is locally available because the axial momentum equation (9) may be integrated, noting that $\mathrm{d}P/\mathrm{d}x$ is constant in the fully developed flow and by symmetry the average shear stress vanishes at the centreline. This yields the shear stress as $\eta_0\eta_s\partial u_x/\partial y = (\mathrm{d}P/\mathrm{d}x)y$. Consequently the solution for ϕ and for $\partial u_x/\partial y$ given the centreline volume fraction, $\phi(0)$, may be determined by a first-order forward Euler scheme; the actual velocity is determined by integrating from $u_x = 0$ at the wall to the centreline after solution for the particle fraction and velocity gradient. To satisfy agreement with the desired bulk fraction, an iteration is performed if the predicted bulk fraction is not within a specified tolerance of the actual ϕ_{bulk}. The iteration procedure, by virtue of the monotonic increase of the centreline volume fraction with ϕ_{bulk}, is straightforward: we assume $\phi(0) \geqslant \phi_{\mathrm{bulk}}$, solve for $\phi(\bar{y})$ as described, and iterate with small increase of $\phi(0)$ until the predicted bulk fraction agrees with that specified. Note that in the experiments, the actual constraint is that the net axial flux of each phase must be constant under steady operation, but there appears to be little difference between this and our constraint on the channel-averaged ϕ for the conditions we have considered.

4. Modelling results and discussion

The model predictions obtained by solution of (8) for the fully developed volume fraction of suspensions at $\phi_{\mathrm{bulk}} = 0.05$, 0.22, and 0.34 as a function of y are presented in figure 6 for $Pe_{\mathrm{B}} = 70$, 550, and 4400. These Pe_{B} correspond, respectively, to nominal dimensional flow rates through the microchannel of 1/8, 1, and 8 $\mu\mathrm{l\,min}^{-1}$. The values of ϕ_{bulk} and Pe_{B} match those of the experimental results shown in figure 4, and to facilitate comparison the experimental results at $Pe_{\mathrm{B}} = 4400$ are also displayed on this plot. The two figures have the same presentation format, although the vertical axes in figure 6 cover a larger range of ϕ. The value of $A = 0.4$ in the function b_i is used in these solutions. The model predicts migration toward the centreline of the channel which is progressively stronger with Pe_{B} for all ϕ_{bulk}, consistent with the experimental observations for the cases of $\phi_{\mathrm{bulk}} = 0.22$ and 0.34. Although the two larger-Pe_{B} curves are very similar, an inset of the central portion of the channel for $\phi_{\mathrm{bulk}} = 0.22$ shows that the difference in ϕ between $Pe_{\mathrm{B}} = 550$ and $Pe_{\mathrm{B}} = 4400$ is over 10% at and near the centreline. Smaller values of A are associated with larger centreline values of ϕ and thus more pronounced total variation, as shown in figure 7 for a suspension of $\phi_{\mathrm{bulk}} = 0.22$ and $Pe_{\mathrm{B}} = 550$.

The predicted variation of ϕ across the channel in figure 6 is qualitatively in agreement with the experiments, although the total variation in ϕ across the channel is stronger than is observed experimentally. However, this deviation may in part

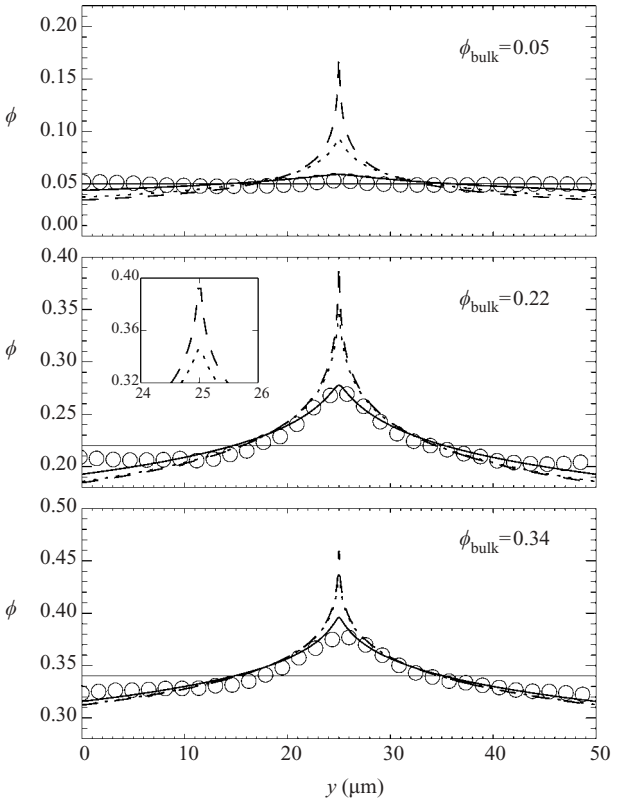

FIGURE 6. Predictions from the flow model of the local volume fraction ϕ in fully developed channel flow as a function of the distance across the channel for $\phi_{bulk} = 0.05$, 0.22, and 0.34 for $Pe_B = 70$ (solid line), $Pe_B = 550$ (dotted) and $Pe_B = 4400$ (dashed). For comparison purposes, note that the conditions match those of the experiments presented in figure 4, and the symbols represent the experimental data at $Pe_B = 4400$ in that figure. The inset in the middle plot illustrates the variation at higher values of Pe_B.

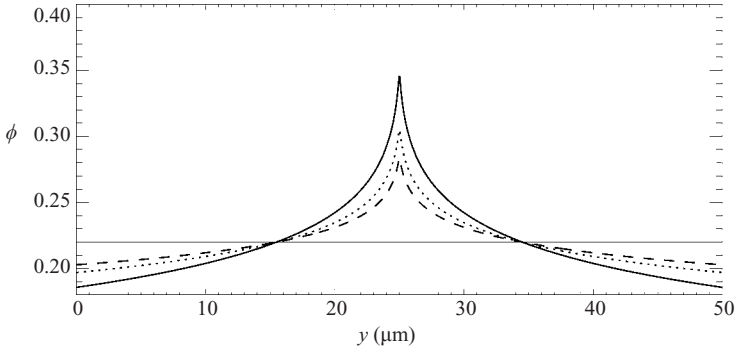

FIGURE 7. Predictions from the flow model of the local volume fraction ϕ in fully developed channel flow at $Pe_B = 550$ and $\phi_{bulk} = 0.22$, for values of $A = 0.4$ (solid line), 0.6 (dotted line), and 0.8 (dashed line).

be due to the application of the model at an arbitrarily small length scale, which leads also to the cusp-like form of the curve $\phi(y)$ at $y = 0$. When the results are averaged over a particle diameter, the discrepancy between predicted and observed

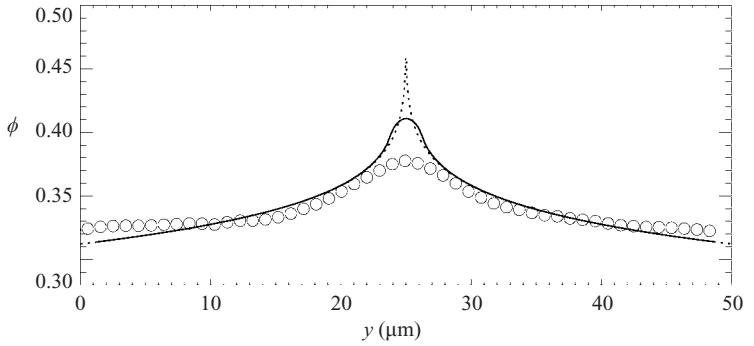

FIGURE 8. Local volume fraction ϕ for the experimental data (symbols), the model prediction (dotted line), and the smoothed model prediction (solid line). The conditions are $\phi_{\text{bulk}} = 0.34$ and $Pe_{\text{B}} = 4400$.

total variation in ϕ is reduced, as is shown in figure 8. While a non-local approach such as that employing normal stresses modelled in terms of suspension temperature (Nott & Brady 1994; Morris & Brady 1998) or using a volume-averaged shear rate (Morris & Boulay 1999) may result in a similar removal of the peak in the profile, it was determined to be preferable to introduce spatially varying Brownian normal stresses in the simplest, i.e. local in $\dot{\gamma}$, version of the model.

The difference between the maximum $\phi(y)$ and ϕ_{bulk} is larger for $\phi_{\text{bulk}} = 0.22$ than for $\phi_{\text{bulk}} = 0.34$ in both experiment and model. In the model, this results from the more close approach of the centreline ϕ to the maximum packing condition when $\phi_{\text{bulk}} = 0.34$; a suspension at ϕ_{bulk} approaching maximum packing would be expected to have very little variation across the channel, a point discussed in Morris & Brady (1998).

We conclude by noting that an additional, and we believe more relevant, factor accounting for the discrepancy between the predicted and observed concentration profiles is the axial dependence of the flow. The model calculations are for the fully developed flow; the experimental observations are taken at a distance $L = 2.6\,\text{cm}$ from the entrance of the channel. While this is far in terms of the particle size ($L/a = 24000$), it is less far in terms of the channel width ($L/H = 520$). Motivated by the discrepancy between the predicted and observed concentration profiles, we checked the experimental axial dependence, and in limited experiments found that the concentration profile continued developing significantly even as far as 3.9 cm from the entrance, the maximum we could measure with the capillary channels available. The scaling of Nott & Brady (1994) suggests full development at $L/H \sim (H/a)^2/\mathscr{D} \sim 2500$, where $\mathscr{D}$ is the self-diffusion coefficient made dimensionless by $\dot{\gamma}a^2$, yielding $L = O(10)\,\text{cm}$. A scaling of (7) yields $L/H \sim (u_x/u_{\max})\delta\phi(H/a)^2/(f\eta_n)$, where $\delta\phi$ is the scale of the change undergone by ϕ. Although this scaling suggests rapid development near the walls, where the velocity is small, it is the most slowly developing region that controls the ultimate approach to fully developed flow, allowing $u_x/u_{\max}$ to be taken as $O(1)$. In this case, the scaling also yields a development length of $O(10)\,\text{cm}$ for the dilute and moderate concentrations which were studied here (at larger ϕ, e.g. $\phi_{\text{bulk}} > 0.45$, the development is predicted to be very rapid as the divergence in η_n is approached). These considerations suggest that future work should investigate this axial dependence to determine the evolution to the fully migrated flow, seek closer agreement with the model profiles, and probe the capability of the model

to predict the developing flow. It is, however, clear that the model and experiments agree in certain important features, including the fact that there is both Péclet number and ϕ dependence in the migration phenomenon.

We thank Gianguido Cianci for helpful discussions. The modelling of normal stresses benefited from the suggestions of Professor Prabhu Nott. The experimental and modelling work were supported (in separate grants to E.R.W. and J.F.M.) by the donors of The Petroleum Research Fund, administered by the American Chemical Society, and the experimental work was supported by the University Research Committee of Emory University.

REFERENCES

Antl, L., Goodwin, J. W., Hill, R. D., Ottewill, R. H., Owens, S. M., Papworth, S. & Waters, J. A. 1986 The preparation of poly(methyl methacrylate) lattices in nonaqueous media. *Colloids Surfaces* **17**, 67.

Batchelor, G. K. 1977 The effect of Brownian motion on the bulk stress in a suspension of spherical particles. *J. Fluid Mech.* **83**, 97.

Bergenholtz, J., Brady, J. F. & Vicic, M. A. 2002 The non-Newtonian rheology of dilute colloidal suspensions. *J. Fluid Mech.* **456**, 239.

Brady, J. F. 1993 The rheological behavior of concentrated colloidal dispersions. *J. Chem. Phys.* **99**, 567.

Brady, J. F. & Morris, J. F. 1997 Microstructure of strongly-sheared suspensions and its impact on rheology and diffusion. *J. Fluid Mech.* **348**, 103.

Brady, J. F. & Vicic, M. A. 1995 Normal stresses in colloidal dispersions. *J. Rheol.* **39**, 545.

Buyevich, Yu. A. & Kapsbov, S. K. 1999 Segregation of a fine suspension in channel flow. *J. Non-Newtonian Fluid Mech.* **86**, 157.

Dinsmore, A. D., Weeks, E. R., Prasad, V., Levitt, A. C. & Weitz, D. A. 2001 Three dimensional confocal microscopy of colloids. *Appl. Optics* **40**, 4152.

Foss, D. R. & Brady, J. F. 2000 Structure, diffusion, and rheology of Brownian suspensions by Stokesian Dynamics simulation. *J. Fluid Mech.* **407**, 167.

Gadala-Maria, F. 1979 The rheology of concentrated suspensions. PhD thesis, Stanford University.

Jeffrey, D. J., Morris, J. F. & Brady, J. F. 1993 The pressure moments for two spheres in a low-Reynolds-number flow. *Phys. Fluids* A **5**, 2317.

Koh, C. J., Hookham, P. & Leal, L. G. 1994 An experimental investigation of concentrated suspension flows in a rectangular channel. *J. Fluid Mech.* **266**, 1.

Krieger, I. M. 1972 Rheology of monodisperse latices. *Adv. Colloid Interface Sci.* **2**, 111.

Leighton, D. T. & Acrivos, A. 1987 The shear-induced migration of particles in concentrated suspensions. *J. Fluid Mech.* **181**, 415.

Leighton, D. T. & Rampall, I. 1993 Measurement of the shear-induced microstructure of concentrated suspensions of non-colloidal spheres. In *Particulate Two-phase Flows* (ed. M. C. Roco). Butterworth-Heinemann.

Lyon, M. K. & Leal, L. G. 1998 An experimental study of the motion of concentrated suspensions in two-dimensional channel flow. I. Monodisperse systems. *J. Fluid Mech.* **363**, 25.

Morris, J. F. & Boulay, F. 1999 Curvilinear flows of noncolloidal suspensions: the role of normal stresses. *J. Rheol.* **43**, 1213.

Morris, J. F. & Brady, J. F. 1998 Pressure-driven flow of a suspension: buoyancy effects. *Intl J. Multiphase Flow*., **24**, 105.

Morris, J. F. & Katyal, B. 2002 Microstructure from simulated Brownian suspension flows at large shear rate. *Phys. Fluids* **14**, 1920.

Nott, P. R. & Brady, J. F. 1994 Pressure-driven suspension flow: Simulation and theory. *J. Fluid Mech.* **275**, 157.

Phung, T. N., Brady, J. F. & Bossis, G. 1996 Stokesian Dynamics simulation of Brownian suspensions. *J. Fluid Mech.* **313**, 181.

Russel, W. B., Saville, D. A. & Schowalter, W. R. 1989 *Colloidal Dispersions.* Cambridge University Press.

van der Werff, J. C. & de Kruif, C. G. 1989 Hard-sphere colloidal dispersions: the scaling of rheological properties with particle size, volume fraction, and shear rate. *J. Rheol.* **33**, 421.

Woodcock, L. V. 1981 Glass transition in the hard sphere model and Kauzman's paradox. *Ann. NY Acad. Sci.* **371**, 274.

Zarraga, I. E., Hill, D. A. & Leighton, D. T. 2000 The characterization of the total stress of concentrated suspensions of noncolloidal spheres in Newtonian fluids *J. Rheol.* **44**, 185–220.